Plasmonic biosensors relying on biomolecular conformational changes: Case of odorant binding proteins

Anil Bozdogan[a,b], **Simone Hageneder**[a], **Jakub Dostalek**[a,*]
[a]AIT-Austrian Institute of Technology GmbH, Tulln, Austria
[b]CEST Kompetenzzentrum für elektrochemische Oberflächentechnologie GmbH TFZ, Wiener Neustadt, Austria
*Corresponding author: e-mail address: jakub.dostalek@ait.ac.at

Contents

Abstract

Plasmonic nanostructures serve in a range of analytical techniques that were developed for the analysis of chemical and biological species. Among others, they have been pursued for the investigation of odorant binding proteins (OBP) and their interaction with

Methods in Enzymology
ISSN 0076-6879
https://doi.org/10.1016/bs.mie.2020.04.068

odorant molecules. These compounds are low molecular weight agents, which makes their direct detection with conventional surface plasmon resonance (SPR) challenging. Therefore, other plasmonic sensor modalities need to be implemented for the detection and interaction analysis of OBPs. This chapter provides a guide for carrying out such experiments based on two techniques that take advantage of conformation changes of OBPs occurring upon specific interaction with their affinity partners. First, there is discussed SPR monitoring of conformation changes of biomolecules that are not accompanied by a strong increase in the surface mass density but rather with its re-distribution perpendicular to the surface. Second, the implementation of surface plasmon-enhanced fluorescence energy transfer is presented for the sensitive monitoring of conformational changes of biomolecules tagged with a fluorophore at its defined part. Examples from our and other laboratories illustrate the performance of these concepts and their applicability for the detection of low molecular weight odorant molecules by the use of OBPs attached to the sensor surface is discussed.

Abbreviations

ATP	adenosine triphosphate
ATR	attenuated total internal reflection
n_s	aqueous sample refractive index
n_b	biolayer refractive index
BRE	biomolecular recognition elements
S_b	bulk refractive index sensitivity
D	diameter
d	distance/thickness
λ_{em}	emission wavelength
EF	electric field enhancement factor
λ_{ex}	excitation wavelength
h	height
HEPES	4-(2-hydroxyethyl)-piperazine-1-ethanesulfonic acid
LSPR	localized surface plasmon resonance
LSPs	localized surface plasmons
OBP	odorant binding protein
Λ	period
PEF	plasmon-enhance fluorescence
PEG	oligoethylene glycol-thiol
L_p	probing depth
PSPs	propagating surface plasmons
RIU	refractive index unit
SAM	self-assembled monolayer
λ_{SPR}	SPR wavelength
SERS	surface plasmon-enhanced Raman spectroscopy
SEIRA	surface-enhanced infrared absorption
SPR	surface plasmon resonance
Γ	surface mass density
TCEP	tris(2-carboxyethyl)phosphine hydrochloride solution
UV-LIL	UV-laser interference lithography
λ	wavelength

1. Introduction

Plasmonics represents a recently established interdisciplinary research domain that concerns tight confinement of light at metallic nanostructures. It exploits resonant excitation of surface plasmons that originate from collective oscillations of electron density. The associated electromagnetic field probes the close proximity of the metallic (typically gold) nanostructures to short sub-wavelength distances. This probing depth can be tuned at a length-scale comparable to the size of a variety of chemical and biological species by the design of the metallic nanostructures. Such tuneable confinement of light energy makes the plasmonic nanostructures ideally suited for optical observation of biomolecules and their interactions at solid surfaces, which have been implemented in a range of biosensor modalities. The measurement of refractive index changes induced by the binding of biomolecules at noble metals is employed in surface plasmon resonance (SPR) biosensors (Homola, 2008; Liedberg, Nylander, & Lundstrom, 1983). The increased intensity of the probing surface plasmon field allows the efficient fingerprinting of molecular analytes in surface plasmon-enhanced Raman spectroscopy (SERS) (Jeanmaire & Van Duyne, 1977; Langer et al., 2019) and it opens doors for in-situ surface-enhanced infrared absorption spectroscopy (SEIRA) (Adato & Altug, 2013) observations of species that are otherwise masked by the absorption of water. Moreover, the plasmonic management of light at the metallic surfaces is utilized for the plasmon-enhance fluorescence (PEF) assays to enhance their sensitivity and suppress the background signal (Bauch, Toma, Toma, Zhang, & Dostalek, 2014).

In the majority of plasmonic biosensors, the detection of target species is performed by the use of biomolecular recognition elements (BRE) that affinity capture target analyte from a liquid sample at the sensor surface. The specific binding is directly monitored through the increased surface mass density (SPR), by the occurrence of specific vibrational bands (SERS, SEIRA) or by using labels (PEF, SERS). In general, all these techniques have been implemented to affinity biosensors for the detection of analytes with medium or large molecular weight. However, their utilization of low molecular weight analytes can be complicated. The SPR approach often does not allow their detection as the small compounds do not induce sufficiently large and thus measurable refractive index change. Likewise, for direct SERS-based analysis, many important low molecular weight analytes are not Raman-active, and the SEIRA approach typically relies on the

amplification of the signal only in a narrow spectral window. Moreover, assays with a fluorophore and Raman-active tags (PEF, SERS) typically rely on a sandwich format that is not suitable for low molecular weight analytes as they do not present two regions to which (typically bulky BREs like antibodies) can simultaneously bind.

To overcome this limitation, BREs that are attached at the sensor surface and undergo a conformational change upon the specific interaction with the target analyte can be utilized. Then, these binding events can be accompanied by a change that is substantially stronger than that induced by the presence of the target analyte itself. For the SPR readout, BRE conformation change can manifest itself as a spatial re-distribution of the surface mass density perpendicular to the surface and be translated to measurable refractive index variations (Hall et al., 2011; Jonsson, Jonsson, Dahlin, & Hook, 2007). Besides, the BRE conformation change can lead to the shifts of its Raman or infrared absorption bands (Jones, Balakrishnan, Squier, & Spiro, 2014; Neumann et al., 2009) and it can be conjugated with a reporting molecule (e.g., fluorophore). Then, the conformation change can be converted to an optical signal based on distance-amended fluorescence quenching (Zheng, Seferos, Giljohann, Patel, & Mirkin, 2009) or SERS signal strength (Jung et al., 2007).

This chapter aims at providing a practical guide to the implementation of two plasmonic sensor modalities for the measurement of conformation changes of biomolecules. In particular, we introduce SPR and PEF approaches relying on the probing of the sensor surface with localized surface plasmons on gold nanoparticles and by propagating surface plasmons traveling along continuous gold films. A possible implementation of such experiments is described by the use of specific protocols. A possible interpretation of the measured optical response due to the refractive index re-distribution on the surface (SPR readout) and due to the plasmon-enhanced fluorescence energy transfer (quenching of PEF) is explained. Lastly, using these techniques in the context of odorant binding proteins (OBP) is discussed. It is worth noting that the analysis of such interactions is a challenge and plasmonic biosensors hold the potential to provide new insights to these studies and can serve in translating this knowledge toward practical applications.

2. Probing of biomolecules at interfaces with surface plasmons

In plasmonic biosensors, the surface of metallic nanostructures carrying analyzed species is probed by the resonantly excited surface

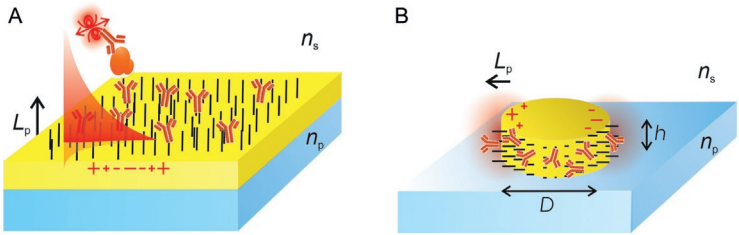

Fig. 1 Schematics of the probing of biomolecular binding events with (A) propagating surface plasmons (PSPs) traveling along a metallic film and (B) localized surface plasmons (LSPs) supported by a metallic nanoparticle with indicated probing depth L_p and refractive index above the structure n_s and below the structure n_p.

plasmons. As illustrated in Fig. 1, two types of surface plasmons can be utilized: (a) propagating surface plasmons (PSPs) that travel along continuous metallic films and (b) localized surface plasmons (LSPs) supported by metallic nanoparticles.

On the surface of gold structures (which are preferably used for their chemical stability and range of surface chemistries available), optical waves at a wavelength in the red and near-infrared parts of the spectrum are often used for the resonant excitation of PSPs and LSPs. For the optical excitation of PSPs, typically, periodically corrugated metallic films or so-called Kretschmann configuration of attenuated total internal reflection (ATR) method are employed. The profile of field for the ATR excited PSPs on a 50 nm thick gold film in contact with water is showed in Fig. 2A. It reveals that at a wavelength of $\lambda = 633$ nm, the PSP electric field intensity peaks at the gold surface (field intensity enhancement of $EF > 30$) and exponentially decays into the adjacent water medium as:

$$|E(z)|^2 = EF \cdot \exp\left(-2d/L_p\right), \tag{1}$$

where EF is the electric field intensity enhancement, d is the distance from the surface and $L_p/2$ is the probing depth. For the PSP field shown, the probing depth of $L_p/2 = 93$ nm was determined.

Significantly tighter confinement of light energy is accompanied by the excitation of LSPs. Fig. 2B shows an example of a cross-section of the LSP electric field intensity for arrays of gold disk nanoparticles (diameter $D = 140$ nm and height $h = 50$ nm) in contact with water. For the geometry with the bottom (substrate) dielectric refractive index of $n_p = 1.46$ that is different from that of water $n_s = 1.33$ on the top, the LSPs are excited at a wavelength of $\lambda = 708$ nm for the period $\Lambda = 360$ nm. Compared to PSPs, a higher enhancement factor of about $EF \sim 100$ occurs due to the

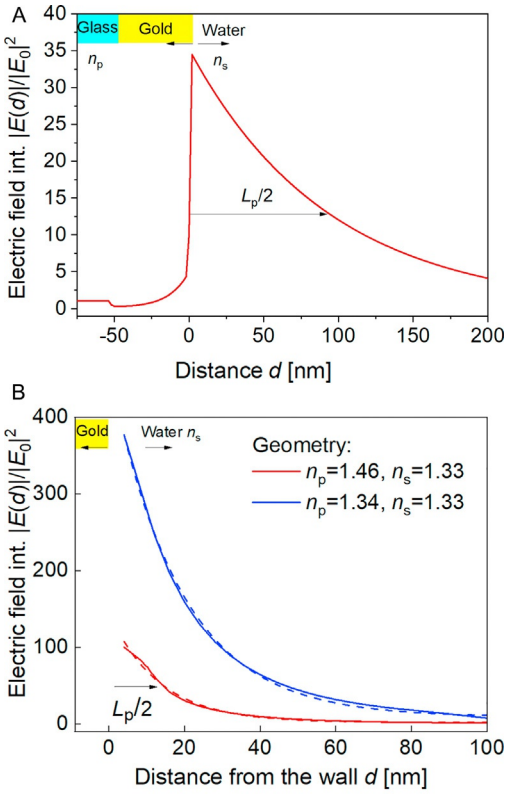

Fig. 2 The profile of the electric field intensity $|E|^2$ normalized with the electric intensity of the excitation optical beam $|E_0|^2$ for (A) resonantly excited PSPs by ATR configuration with a 50 nm thick gold film in contact with water (refractive index of $n_s = 1.33$) at a wavelength of 633 nm and (B) LSPs on arrays of cylindrical nanoparticles with a diameter of $D = 140$ nm and height $h = 50$ nm in the refractive index asymmetrical (refractive index of the substrate of $n_p = 1.45$, period of $\Lambda = 360$ nm) and nearly symmetrical geometry (refractive index of the substrate of $n_p = 1.34$, period of $\Lambda = 525$ nm). Solid lines correspond to finite difference time domain simulations and dashed lines are exponential fits.

tighter confinement of the field featuring $L_p/2 = 13$ nm. Interestingly, the probing depth L_p can be substantially increased by adjusting the nanoparticle arrays period to $\Lambda = 525$ nm and setting the refractive index of the bottom dielectric to $n_p = 1.34$ (so it is close to that above water with $n_s = 1.33$). In such refractive index symmetrical geometry, so-called lattice LSPs can be excited and the presented example in Fig. 2B reveals an increased electric field intensity enhancement factor of $EF \sim 400$ and a less localized field with a probing depth of $L_p/2 = 18$ nm.

The optical coupling to PSPs and LSPs is typically manifested as a dip in the reflectivity or transmission wavelength spectrum centered at a wavelength λ_{SPR}, where part of the light energy is resonantly transferred to surface plasmon modes. This energy is partially dissipated in the metal due to the Ohmic losses, which, as Fig. 3 illustrates, affects the spectral width of the resonant dip $\Delta\lambda$. An example of the SPR dip in the reflectivity spectrum for the PSP excitation on a gold film is showed in Fig. 3A; an SPR dip in the transmission spectrum for LSPs excitation on arrays of gold cylindrical nanoparticles can be seen in Fig. 3B.

Importantly, the spectral position of the SPR dip λ_{SPR} in reflectivity or transmission spectra shifts with the changes in refractive index n_s of the

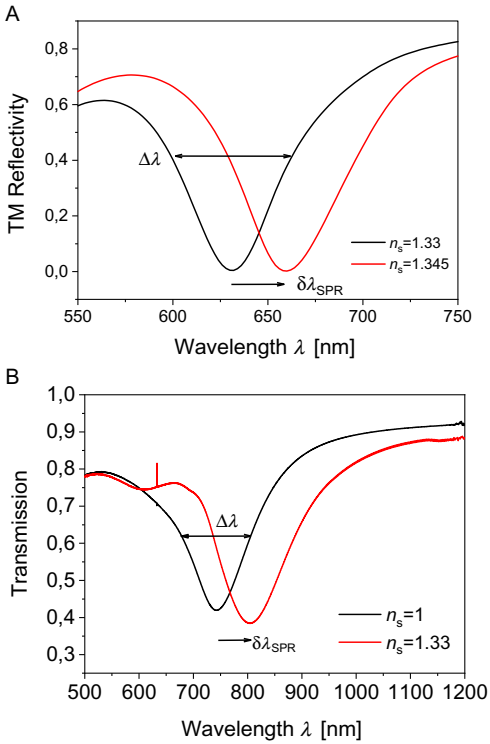

Fig. 3 Refractive index sensitivity for (A) ATR excitation of PSP modes with wavelength interrogation and (B) for the transmission measurement of resonant excitation of disk nanoparticle arrays. The excitation of PSP is simulated in transversally magnetic (TM) reflectivity for a prism with $n_p = 1.845$, 50 nm thick Au layer, water on the top, and angle of incidence of $\theta = 51.7$ deg. (B) Measured LSPR spectra for the resonant coupling to LSPs for normal angle of incidence of $\theta = 0$ on gold arrays of gold disk nanoparticles with a diameter $D = 175$ nm, height $h = 50$ nm, and period $\Lambda = 460$ nm on a glass surface with $n_p = 1.5$.

dielectric adjacent to the metal. These spectral shifts are linear for small changes δn_s and can be quantified by a bulk refractive index sensitivity S_b. For the examples shown, the bulk refractive index sensitivity for the wavelength interrogation of resonantly excited PSPs in ATR configuration is $S_b = \delta\lambda_{SPR}/\delta n_s = 2000\,\text{nm/RIU}$ (unitless RIU states for refractive index unit). For the resonant coupling to LSPs, the bulk refractive index is one order of magnitude smaller and $S_b = 190\,\text{nm/RIU}$ was measured in the presented experiment.

The metallic structures for the resonant excitation of PSPs and LSPs are typically prepared on glass substrates by a combination of thin-film deposition and lithography. The following protocol describes the use of thermal evaporation and UV-laser interference lithography (UV-LIL) for the preparation of continuous thin gold films (supporting PSPs) and arrays of cylindrical gold nanoparticles (supporting LSPs). For illustration, the procedure is summarized in Fig. 4.

2.1 Definition

Preparation of plasmonic nanostructures by UV-interference lithography.

2.2 Rationale

Metallic nanostructures and metallic thin films are deployed on the surface of plasmonic sensors to optically probe the reactions of biomolecules occurring on their top when contacted with analyzed liquid samples.

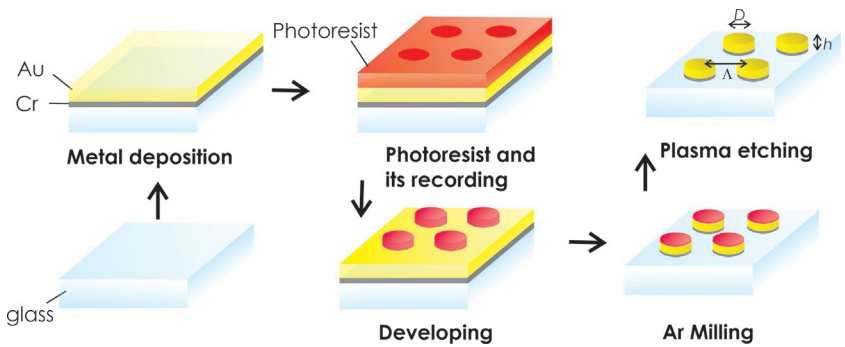

Fig. 4 Schematics of steps in the preparation of arrays of cylindrical gold nanoparticles on a glass substrate.

2.3 Materials, equipment, and reagents

- Microposit S1805 G2 positive photoresist (Micro Resist Technology, Germany)
- Propylene glycol monomethyl ether acetate (PGMEA, Sigma Aldrich, Germany)
- Developer AZ 303 (Micro Resist Technology, Germany)
- Au granules and Cr powder (Mateck, Germany)
  - Vacuum thermal evaporation instrument (HHV AUTO 306 from HHV LTD, UK)
  - Spincoater G3P-8 (Pi-Chem, UK)
  - UV-interference lithographer with a 4 mW HeCd laser (model IK 3031 R-C from Kimmon, Japan) emitting at a wavelength $\lambda = 325$ nm coherent beam and Lloyds mirror configuration, details can be seen in publications (Khan, Keshmiri, Kolb, Dimopoulos, & List-Kratochvil, 2016; Quilis et al., 2018)
  - Argon milling system IonSys 500 (Roth & Rau, Germany)
  - Oxygen plasma etcher

2.4 Protocol

(1) Subsequent deposition of 2 nm Cr and 50 nm Au layers in vacuum better than 10^{-6} mBar from tungsten and molybdenum boats, respectively, deposition rate 0.1 Å/s.

(2) Deposition of S1805 G2 photoresist solution diluted 1:2 with propylene glycol monomethyl ether acetate by the use of spin-coating at 4500 rpm for 45 s, followed by a soft baking step at 100 °C on a hot plate for 120 s.

(3) Recording of the UV-interference pattern to prepared 100 nm thick photoresist layer, irradiation power 30 μW/cm^2, irradiation dose of 6.75 mJ/cm^2.

(4) Developing the structure recorded to the photoresist layer by AZ 303 developer diluted with distilled water at a ratio 1:15. Typical developing time is between 90 and 240 s.

(5) Directional dry etching with an argon milling is applied to transfer the pattern from the resist into the underlying Au layer (etching time 450 s, 70 degrees).

(6) Finally, the remaining resist is removed using oxygen plasma at 1 mbar and 40 W applied for 5 min.

Pros	Cons
Structuring over the large surface area	The geometry of metallic nanoparticles is restricted to cylindrical and elliptical shapes
Well-ordered period arrays of metallic nanoparticles	
Tuneable geometry characteristics—period and diameter of the arrays	

2.5 Alternative methods/procedures

Plasmonic nanostructures can be alternatively prepared by electron beam and focused ion beam lithography, which allow for the fabrication of an almost arbitrary shape of nanoparticles. However, these methods are time-consuming and not suitable for routine use in analytical technologies as structuring areas larger than 100 μm is complicated and complex infrastructure is required.

Moreover, colloidal lithography can be employed for facile structuring of large areas. Wet chemical synthesis of metallic nanoparticles also provides efficient routes for the cost-efficient preparation of metallic nanostructures. However, these methods lack the possibility to arrange the structures in perfect lattices.

2.6 Troubleshooting and optimization

Problem	Solution
Metallic nanoparticles are connected	Increase the irradiation dose or development time
Metallic nanoparticles are not present	Often due to the over-etching during the ion milling step

2.7 Summary

UV-interference lithography—UV-LIL—is a method able to combine the advantages of large-area structuring and relatively high throughput and it is suitable for the routine preparation of plasmonic nanostructures whenever perfect lattice arrangement is required. If needed, it can be employed for the preparation of master structures for subsequent UV-nanoimprint lithography when scaling up of the production is important.

3. Monitoring of biomolecule conformation changes by SPR

In SPR biosensors, the kinetics of surface reactions can be monitored by the tracking of variations of SPR wavelength λ_{SPR} due to the binding-induced refractive index changes. Series of transmission or reflectivity spectra are acquired in time, and by their analysis, the SPR wavelength detuning is determined as a shift of the SPR dip minimum. Typically, it is determined by fitting the spectrum with an analytical function or by using a centroid approach. These methods provide accuracy in the λ_{SPR} baseline measurement with the noise of $\sigma(\lambda_{SPR}) = 10^{-2} - 10^{-3}$ nm (Dahlin, Tegenfeldt, & Hook, 2006; Reiner et al., 2017).

In regular SPR measurements, changes in λ_{SPR} due to the increase of the surface mass density Γ that is ascribed to the capture of target analyte on the sensor surface are monitored:

$$\Gamma = d(n_b - n_s)\frac{\partial c}{\partial n}, \tag{2}$$

where n_b states the refractive index of a biolayer (representing the BRE and the captured analyte), d represents its thickness, and the coefficient $\partial n/\partial c = 0.2\,\mathrm{mm^3\,mg^{-1}}$ relates the changes in refractive index with the concentration of biomolecules bound to the surface. (Stenberg, Persson, Roos, & Urbaniczky, 1991)

The SPR wavelength shift $\delta\lambda_{SPR}$ due to refractive index changes of the biolayer n_b depends on its thickness as the probing field exponentially decreases with a characteristic probing depth $L_p/2$ (see Fig. 2). The SPR wavelength shift induced by the formation of a biolayer with a thickness d and refractive index n_b can be mathematically expressed based on perturbation theory (Snyder & Love, 1983) as:

$$\delta\lambda_{SPR} = S_b \int_0^d (n_b - n_s)|E(z)|^2 dz \Big/ \int_{-\infty}^{\infty} |E(z)|^2 dz. \tag{3}$$

This equation can be further simplified when using the penetration depth of the probing field L_p as follows:

$$\delta\lambda_{SPR} \sim S_b(n_b - n_s)\left(1 - e^{-2d/L_p}\right) = S_b\Gamma\frac{\partial n}{\partial c}\frac{1 - e^{-2d/L_p}}{d}. \tag{4}$$

In general, the SPR wavelength shifts not only when the surface mass density Γ is increased due to the capture of biomolecules on the metallic surface, but also when the biolayer is redistributed in a way that its overall surface mass density Γ stays constant (e.g., by increasing its thickness d and decreasing its refractive index $n_{p,}$ so the $d/(n_b\text{-}n_s)$ is not changed). If the limit of the biolayer thickness much lower than the surface plasmon probing depth $d \ll L_p$, Eq. (4) yields:

$$\delta\lambda_{SPR} = S_b \Gamma \frac{\partial n}{\partial c} \frac{2}{L_p}, \tag{5}$$

and for the opposite situation when $d \gg L_p$ this equation holds

$$\delta\lambda_{SPR} = S_b \Gamma \frac{\partial n}{\partial c} \frac{1}{d}. \tag{6}$$

The sensitivity of SPR wavelength λ_{SPR} to the re-distribution of the biolayer mass in the direction perpendicular to the metal surface can be exploited for the observation of conformational changes of biomolecules. In principle, the conformational change can manifest itself as a change of respective biolayer refractive index n_p and thickness d. If the distance range at which this re-distribution occurs (represented by the effective thickness of the biolayer d) is larger or comparable with the surface plasmon probing depth $d \sim L_p$, such change can translate to a measurable shift in λ_{SPR}. Fig. 5A shows simulations that elucidate such an experiment. In this example, a shift of SPR wavelength λ_{SPR} due to the formation of a biolayer with a thickness of $d_0 = 10$ nm was determined for the probing depth of $L_p/2 = 100$, 10, and 1 nm by using Eq. (4). Then, the surface mass density of the layer Γ was assumed constant and the changes in the SPR wavelength were determined for its thickness d varied between 5 and 15 nm (and refractive index n_b concluded from Eq. 2). The simulated SPR wavelength $\lambda_{SPR}(d)$ was normalized to that determined for the original thickness $\lambda_{SPR}(d_0)$. These data predict that for the probing depth of $L_p/2 = 100$ nm (representing PSP—see Fig. 2A) and $L_p/2 = 10$ and 1 nm (representing LSPs—see Fig. 2B), a 10% change in the biolayer thickness translates to a change in the SPR wavelength λ_{SPR} of about 0.5%, 5%, and 10%, respectively, when compared to that corresponding to the initial biolayer.

To illustrate the above theory, let us relate it to the results reported by the van Duyne laboratory on the conformational change of calmodulin. It is a protein with a prolonged shape with a characteristic length of about 6.5 nm that increases by about 1 nm (corresponding to about 15%) upon its

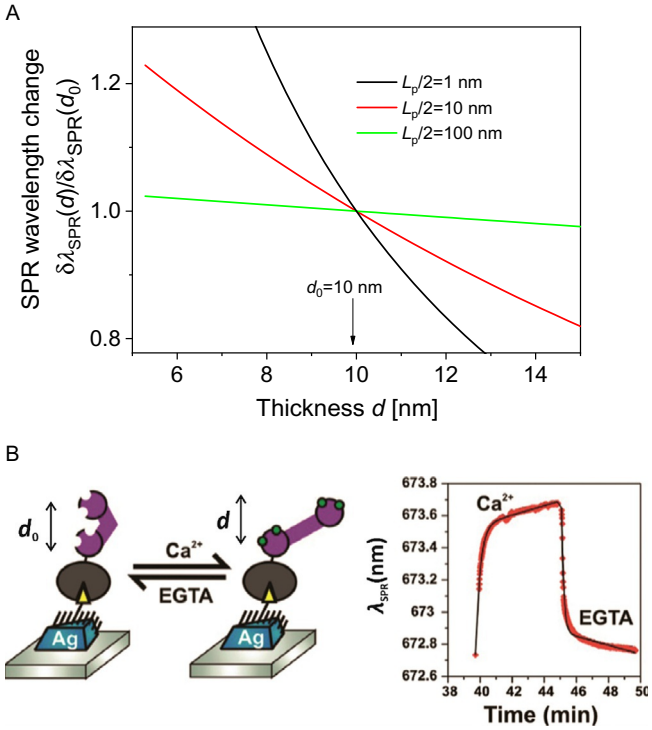

Fig. 5 (A) Simulations of the SPR wavelength changes induced by a conformational change of a biomolecule represented by variations of a biolayer characteristic thickness of $d_0 = 10$ nm in the range $d = 5$–25 nm for three surface plasmon probing depths $L_p/2$ stated in the graph. (B) Example of a conformation change of a protein calmodulin observed by tracking of LSPR wavelength changes. Adapted with permission from (Hall et al., 2011). Copyright 2011 American Chemical Society.

interaction with calcium ions (Hall et al., 2011). This conformation change was observed on silver triangular nanoparticles with the LSPR probing depth of $L_p/2 = 5$–10 nm. The immobilization of calmodulin protein on the sensor carrying a thiol SAM linker layer induced a shift in the LSPR wavelength of $\delta\lambda_{SPR}(d_0) = 3.8$ nm. Upon the interaction with Ca^{2+}, a change up to 0.9 nm was observed in $\delta\lambda_{SPR}$ (corresponding to 23%). These observations are in qualitative agreement with the above-presented model, taking into account the uncertainties in the conformation change on the surface and in bulk as well as in the probing field depth $L_p/2$. It is worth noting that these observations were made possible by an instrument that allowed for accurate tracking of the LSPR wavelength changes with a baseline standard deviation of $\sigma(\lambda_{SPR}) = 2 \times 10^{-3}$ nm.

4. Monitoring of biomolecule conformation changes by PEF

An alternative approach to the monitoring of conformational changes can be utilized based on the fluorescence energy transfer that occurs at close proximity to metals. This phenomenon leads to strong quenching of emitted fluorescence light at distances below or comparable with a Förster distance of 10–15 nm. It is worthy of noting that such distance-dependent quenching of fluorescence depends on the orientation of the fluorophore (see Fig. 6) and that in most common experiments the measured signal is averaged over all possible orientations.

On a gold surface, the distance-dependent fluorescence quenching of a fluorophore attached to a BRE can be implemented for the monitoring of its conformation changes induced by the affinity interaction with a target analyte, see Fig. 7. The additional interaction of the emitter with surface plasmons at the excitation wavelength λ_{ex} (close to the spectral position of the fluorophore absorption band) and emission wavelength λ_{em} offers means to enhance the strength of the detected fluorescence signal and to control the angular distribution of the emitted light. In the example presented in Fig. 7, an aptamer hairpin was used as BRE for a low molecular weight analyte and it was designed with an Alexa Fluor 647 fluorophore attached to its 5′ end with a thiol group at its 3′ end (Sergelen et al., 2017). The aptamer was composed of two key sequences that partially

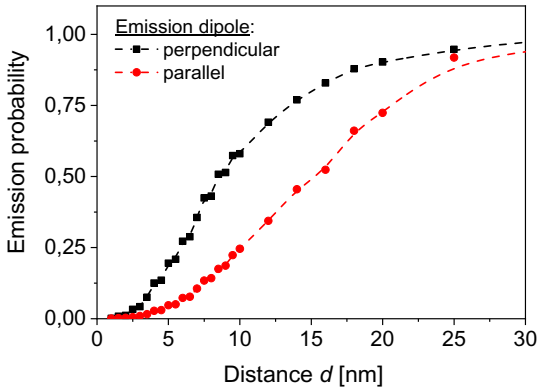

Fig. 6 Simulations of emission probability of a fluorophore represented as a dipole radiating at a wavelength of $\lambda = 670$ nm above a gold surface in contact with water. Emission probability to the far-field radiation propagating in water was simulated.

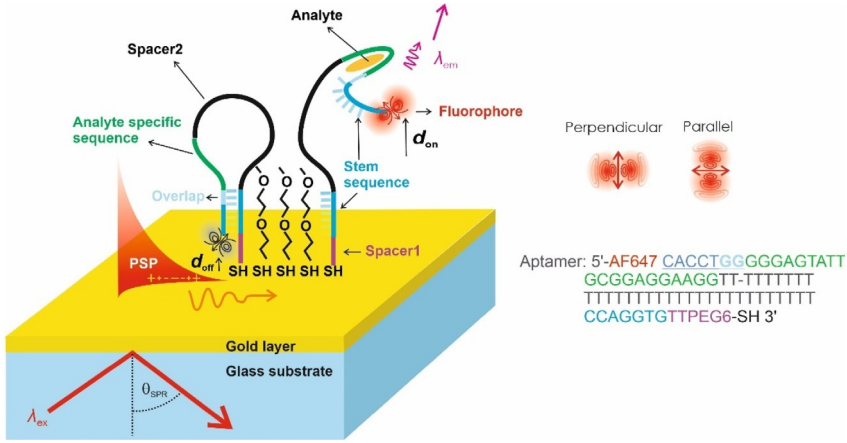

Fig. 7 Schematics of the aptamer-based assay on the gold sensor surface that utilizes a fluorophore coupled with propagating surface plasmons (PSP). The hairpin aptamer was anchored at the gold surface via a thiol group at the 3′ end and the surface density was diluted by using polyethylene glycol-thiol (PEG) for the affinity capture of target analyte—adenosine triphosphate. *Reproduced with permission from Sergelen, K., Fossati, S., Turupcu, A., Oostenbrink, C., Liedberg, B., Knoll, W., et al. (2017). Plasmon field-enhanced fluorescence energy transfer for hairpin aptamer assay readout.* ACS Sensors, *2(7), 916–923. Copyright 2017 American Chemical Society.*

overlap: a stem sequence and analyte-specific sequence. The stem sequence leads to a formation of a hairpin of the aptamer oligonucleotide chain in the absence of the target analyte. When the aptamer is anchored to a gold surface via the 3′ end with the thiol group, the fluorophore attached to the opposite aptamer 5′ end is present in the close proximity to the surface and thus is strongly quenched (see the rapidly decreasing emission probability when lowering the distance d in Fig. 6). Upon the affinity binding of the target analyte (low molecular weight adenosine triphosphate—ATP—was used in the discussed example), the stem sequence interaction is disrupted and the aptamer takes an open-loop structure. As can be seen in Fig. 8, the fluorescence signal then strongly increases as the fluorophore is lifted from the gold surface up. These measurements were carried out with the ATR configuration for the excitation of PSP modes with a monochromatic optical beam at a wavelength of $\lambda_{ex} = 633\,nm$ coinciding with the absorption band of the used fluorophore Alexa Fluor 647. As can be seen in Fig. 8B, the affinity binding of ATP analyte at the gold sensor surface with aptamer hairpin leads to an occurrence of a strong fluorescence peak measured at the fluorophore emission wavelength $\lambda_{em} = 670\,nm$. The peak occurs at an angle of

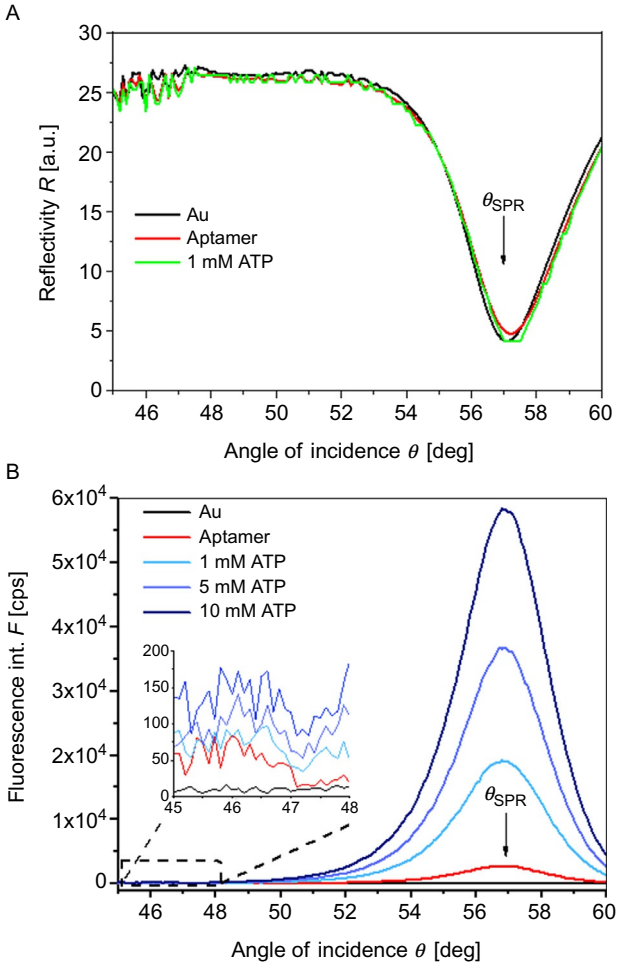

Fig. 8 (A) Angular SPR reflectivity spectra $R(\theta)$ and (B) respective fluorescence intensity spectra $F(\vartheta)$ measured for a hairpin aptamer BRE attached at the sensor surface that was brought in contact with a sample spiked with concentrations of a target analyte—ATP—of 0, 1, 5, and 10 mM. The gold sensor surface was functionalized with a long loop ATP hairpin aptamer (see schematics in Fig. 7). *Reproduced with permission from Sergelen, K., Fossati, S., Turupcu, A., Oostenbrink, C., Liedberg, B., Knoll, W., et al. (2017). Plasmon field-enhanced fluorescence energy transfer for hairpin aptamer assay readout.* ACS Sensors, *2(7), 916–923. Copyright 2017 American Chemical Society.*

incidence of the excitation beam with λ_{ex} at which PSP modes amplify the fluorescence signal emitted away from the gold sensor surface. When increasing the concentration of target analyte, the peak fluorescence signal is increasing as a higher fraction of the aptamer BREs on the surface is switched to the open-loop configuration. Interestingly, the regular SPR

response presented in Fig. 8A shows no measurable change due to the ATP induced conformation change of the aptamer (at a distance range $d < 10\,\text{nm}$), as the probing depth is much larger ($L_p/2 = 93\,\text{nm}$).

4.1 Definition

Surface plasmon resonance—SPR—combined with plasmon-enhanced fluorescence—PEF—spectroscopy.

4.2 Rationale

The combination of SPR and PEF techniques can serve for in-situ characterization of biointerfaces and for the monitoring of affinity binding events of high and low molecular analytes. In conjunction with appropriate models, the kinetic data can be analyzed in order determine binding rates and equilibrium affinity constants.

4.3 Materials, equipment, and reagents

- (11-Mercaptoundecyl)triethylene glycol (PEG-thiol, SPT-0011) from SensoPath Technologies (USA)
- DNA ATP hairpin aptamer with a fluorophore at one and anchoring thiol group at the other end. An example is AlexaFluor 647N 5′-CA CCT GGG GGA GTA TTG CGG AGG AAGGTT TTT TTT TTT TTT TTT TTT TTT TTT TTT CCAGGT G TT PEG6-SH 3′ synthesized by IDT-DNA (Leuven, Belgium)
- All additional chemicals are by Sigma Aldrich, Austria:
  - Tris buffer (10 mM Tris hydrochloride + 6 mM $MgCl_2$, pH 7.4)
  - HEPES buffer (10 mM 4-(2-hydroxyethyl)-piperazine-1-ethanesulfonic acid containing 150 mM NaCl, 5 mM MgCl2, and 0.005% Tween 20, pH 7.4)
  - Tris(2-carboxyethyl)phosphine hydrochloride solution (TCEP)
  - Adenosine, guanosine and adenosine 5′-triphosphate (ATP) disodium salt hydrate
- Optical setup relying on Kretschmann configuration of ATR for combined SPR and PEF experiments: A He-Ne laser (2 mW) emitting at $\lambda_{ex} = 633\,\text{nm}$ is coupled to a prism made of high refractive index glass LASFN9 (exhibiting $n_p = 1.845$) with optically matched glass substrate carrying gold layer. The enhanced electromagnetic field intensity associated with the resonant excitation of PSPs at λ_{ex} excites Alexa Fluor 647 fluorophores and the emitted fluorescence light at the emission wavelength $\lambda_{em} = 670\,\text{nm}$ is collected from the direction perpendicular to

the surface. The emitted fluorescence light beam is spectrally cleaned by using a notch filter (XNF-632.8-25.0M from CVI Melles Griot) and bandpass filter (670FS10–25 from Andover Corporation Optical Filter) and its intensity F is detected by using an avalanche photodiode (Count-200-FC, Laser Components, Germany) or photomultiplier tube. More details can be found in the publication (Sergelen et al., 2017) and Fig. 9.

4.4 Protocol

(1) Freshly prepared borosilicate or LASFN9 glass substrates with a layer of 2 nm chromium and 50 nm gold or with arrays of gold nanoparticles (see protocol above).

(2) Incubation of the substrates in a 1 μM solution of ATP aptamer in Tris buffer.

(3) Optically matching the substrate to a LASFN9 glass prism by using refractive index matching oil (from Cargille, USA), clamping a flow cell on top and connecting the cell to a pump. Mounting into the SPR/PEF optical setup.

(4) Incubation of the substrates in TCEP (100 μM) for 4 h for reduction of the aptamer.

(5) Addition of 10 μM PEG-thiol to the solution and incubation for 2 h form a self-assembled monolayer (SAM).

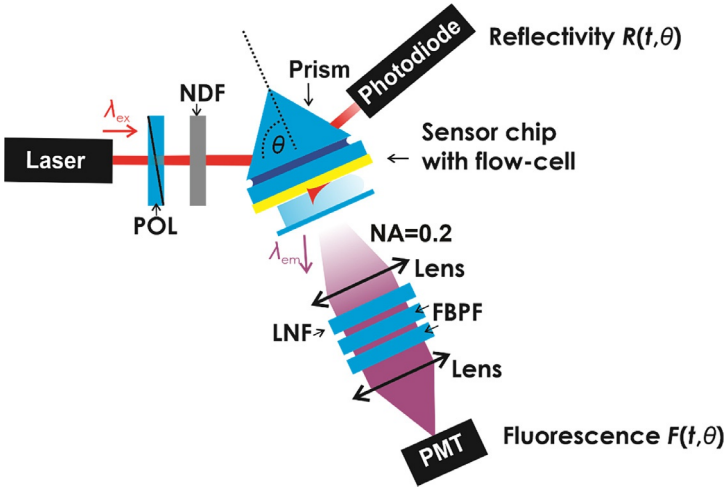

Fig. 9 Optical setup for combined SPR and SPFS measurement: Polarizer (POL), laser notch filter (LNF), fluorescence bandpass filter (FBPF), and photomultiplier (PMT). The systems can measure reflectivity R and fluorescence intensity F depending on the angle of incidence θ and time t.

(6) Washing of the sensor surface for 15 min with Tris or HEPES buffer.
(7) Sequential injection of the target analyte (ATP) and reference analytes for 3 min in either Tris or HEPES buffer with real-time monitoring of fluorescence signal F emitted upon the resonant excitation of PSPs at a wavelength λ_{ex} that is close to the absorption band of the used fluorophore.

Pros	Cons
Real-time observation of biomolecular interaction kinetics	Often unspecific interactions complicate the measurements
Possible monitoring of both low and high molecular weight analytes	Identification of affinity captured species can be done only in combination with other techniques such as mass spectrometry
Parallel screening of multiple interactions available by multichannel devices or in combination with microarrays	

4.5 Alternative methods/procedures

Direct monitoring of affinity surface reaction kinetics can be performed by quartz crystal microbalance (QCM) or optically by methods including reflectometric interference spectroscopy (RIFS) and integrated waveguide Mach Zehnder interferometry.

4.6 Troubleshooting and optimization

Problem	Solution
Analysis of complex samples often complicates the blocking of the sensor surface with abundant components present in complex analyzed samples	Design of biointerface by using polymer surface architectures that exhibit antifouling properties. Using buffers with blocking agents at a high concentration such as BSA or Tween 20
Need of parallel analysis of multiple reactions on the surface	SPR and PEF can be combined with microarray detection format, and a range of multichannel sensors is commercially available based on, e.g., surface plasmon imaging (SPRI)

4.7 Summary

The combination of SPR and PEF provides a versatile platform for the monitoring of affinity interaction of a wide spectrum of analytes ranging from high to low molecular weight biomolecules. Besides, it can be employed as a quality control for the development of biointerface preparation protocols as well as to support the overall process of assay development for the identifying of a suitable biomolecular recognition element, implementing biointerface architecture, and optimizing concrete assay steps.

5. Context of odorant binding protein interaction

Odorants represent an important class of low molecular weight analytes (up to 300 Da) that recently attracted attention of the biosensor research community aiming at mimicking the smell functionality of insects and vertebrates (Pelosi, Mastrogiacomo, Iovinella, Tuccori, & Persaud, 2014). They are highly hydrophobic molecules and they are transferred across the mucosa in vertebrates and trigger a cascade of reactions including those with olfactory receptors on a lipid membrane of nasal epithelial cells. Odorant binding proteins—OBPs—are present in the mucosa to capture hydrophobic odorants and to facilitate their transport to the olfactory receptors. OBPs are medium-sized proteins between 10 and 30 kDa and they have been proposed to serve as a BREs for the low molecular weight odorants (Larisika et al., 2015) based on their conformational change. The OBPs of vertebrates exhibit a structure of eight antiparallel β-sheets and a short α-helical segment. Their conformation change upon the affinity capture of odorants has been subjected of numerous studies including molecular dynamics simulations of rat and pig OBPs (Hajjar, Perahia, Debat, Nespoulous, & Robert, 2006) combined with circular dichroism measurements (Nespoulous, Briand, Delage, Tran, & Pernollet, 2004) and protein crystallography (White, Briand, Scott, & Borysik, 2009). These studies indicate that the size of the OBPs is several nanometres and that their overall structure is still preserved upon the capture of odorant molecules in their binding pocket. The distance between different domains can vary subtly, still, according to our knowledge, this change has not yet been exactly quantified in terms of, e.g., hydrodynamic radius or mass distribution change.

Hurot et al. reported a biosensor for odorant molecules using rat OBPs and SPR sensor configuration relying on ATR to probe its gold surface with

PSP modes at a wavelength of 663 nm (Hurot et al., 2019). Three genetically mutated rat OBP proteins were modified to carry a cysteine group at their N-terminus allowing the formation of a self-assembled monolayer on the gold sensor surface with a surface mass density of about $\Gamma \sim 2000\,\mathrm{pg/mm^2}$ (deduced from the reported surface density of 6×10^{12} proteins/cm^2 and molecular weight of 20 kDa). These OBPs were spotted in a microarray format, including an OBP3-w natural protein (recognizing odorant molecules with a benzene ring structure), mutated OBP3-a (designed for interaction with aldehydes with increased affinity), and control OBP3-c. Afterward, the sensor surface was exposed to aqueous solutions with the dissolved odorant molecules β-ionone, hexanal, and control hexanoic acid. The affinity binding of these compounds was monitored from detuning of the SPR signal with an instrument providing the resolution of $\delta\Gamma = 5\text{–}10\,\mathrm{pg/mm^2}$. The binding of the odorant molecules gave a specific response for even sub nM concentrations. The authors speculate that this can be ascribed to an amplification mechanism related to the conformational change of OBP. For the probing depth of the PSP field of about $L_p/2$–100 nm and assuming the model presented in Fig. 5, the measurable conformation change with the instrument would need to be above 5% of the effective thickness change of the OBP protein layer. It should be noted that the SPR change due to the mass increase associated with the capture of the target itself analyte is not measurable (corresponding to $\Gamma = 5\text{–}10\,\mathrm{pg/mm^2}$ when all OBPs capture one odorant molecule).

An alternative approach to detect odorant molecules by SPR was reported by (Cennamo et al., 2015). This work also employed an SPR detection principle based on the probing of the gold sensor surface with PSP modes at a wavelength of about 640 nm with a miniature fiber optic probe. Such a platform does not typically allow resolving as small changes in surface mass density $\delta\Gamma$ as the previous ATR-based example; thus a competitive assay was developed. The gold surface was chemically modified with thiol self-assembled monolayer carrying carboxyl groups that were subsequently used for attaching of butyric acid by amine coupling. This compound has a similar chemical structure to the odorant molecule butanal and can be recognized by porcine OBP dissolved in an aqueous solution in contact with the sensor. By spiking the analyzed sample containing target butanal with the porcine OPB, the butanal concentration-dependent response is obtained. It is based on the blocking of the binding pocket of the OBP with butanal that hinders its affinity interaction with butyric acid on the surface. According to the obtained data, a limit of detection of 25 μM was achieved by such an indirect measurement.

The third example of the detection of odorant molecules by a plasmonic biosensor relies on the use of gold nanostructures that support more confined LSP modes for direct detection. Zhang et al. developed a plasmonic nanostructure consisting of a thin gold film that was perforated with arrays of nanoholes (Zhang et al., 2015). The gold forms small metallic nanoclusters with a characteristic size of about 20 nm. The nanoholes allow the excitation of LSPs with a tightly confined probing depth $L_p/2$ of less than 10 nm. On the surface of this structure honey bee Acer-ASP2 OBP was immobilized by a thiol SAM through amine coupling, leading to a shift of the LSPR wavelength $\delta\lambda_{SPR}$ of 23 nm. To directly detect the target odorant—β-ionone—the changes in an LSPR wavelength $\delta\lambda_{SP}$ associated with the conformation change of the used OBP were monitored. The β-ionone interaction with the OBP serving as a BRE at the sensor surface was measured by the analysis of transmission intensity and LSPR wavelength shifts. The observed shift in the LSPR wavelength λ_{SPR} of 10–20 nm was observed upon increasing odorant concentration from 10 nM to 1 mM. With respect to the model presented in Fig. 5, such a strong response cannot be solely explained by the conformational change of the OBP (when compared to that for the immobilization of the OPB itself which reached similar value). In order to fully explain these measurements, more detailed information needs to be acquired, e.g., measuring the affinity binding kinetics by accurately tracking the respective changes in the LSPR wavelength λ_{SPR} to be able to distinguish the specific response from other effects.

6. Summary

This chapter presents an implementation of two plasmonic biosensor techniques for the investigation of affinity interaction of low molecular weight molecules with their ligands attached at a solid surface. The possible utilization of conformational changes occurring upon such interaction for sensitive target analyte detection is discussed. In the field of odorant biosensors relying on odorant binding proteins, there has been used SPR-based monitoring of conformational changes that are accompanied with the re-distribution of the surface mass density perpendicular to the sensor surface. We discuss the accuracy of this approach and how it depends on the probing depth of the surface plasmon field, which can be controlled by the choice of the metallic nanostructures that support surface plasmon modes (either propagating or localized). A practical guide for the preparation of metallic nanostructures with controlled plasmonic properties and possible means to modify their surface

with biorecognition elements are given and the performance of plasmonic biosensors relying on the OBP conformational changes is illustrated by selected examples from literature. In addition, an approach based on plasmon-enhanced fluorescence energy transfer is introduced and its utilization presented for biomolecular recognition elements, which can be selectively tagged with a fluorophore at their defined parts. The conformation change due to the capture of a low molecular weight target analyte is then accompanied by a change in the distance between the fluorophore and the metal, leading to strong fluorescence signal variations. This sensitive approach was not yet explored for detection of odorant molecules, but may become an attractive modality in conjunction with recently explored alternatives to OBPs based on synthetically made DNA and peptide hairpin biomolecular recognition elements capable to specifically capture odorant molecules (Gaggiotti et al., 2020).

Acknowledgment

S.H. and J.D. received support from the European Union's Horizon 2020 research and the innovation program under Grant Agreement No. 633937, project ULTRAPLACAD, the Austrian Research Promotion Agency (FFG) with grant agreement No. 861578 (ERANET project PLABAN), and by Lower Austria EFRE project IKTHEUAP (WST3-F-5030820/010-2019).

References

Adato, R., & Altug, H. (2013). In-situ ultra-sensitive infrared absorption spectroscopy of biomolecule interactions in real time with plasmonic nanoantennas. *Nature Communications*, *4*, 2154. https://doi.org/10.1038/ncomms3154.

Bauch, M., Toma, K., Toma, M., Zhang, Q., & Dostalek, J. (2014). Plasmon-enhanced fluorescence biosensors: A review. *Plasmonics*, *9*, 781–799.

Cennamo, N., Di Giovanni, S., Varriale, A., Staiano, M., Di Pietrantonio, F., Notargiacomo, A., et al. (2015). Easy to use plastic optical fiber-based biosensor for detection of Butanal. *PLoS One*, *10*(3), e0116770. https://doi.org/10.1371/journal.pone.0116770.

Dahlin, A. B., Tegenfeldt, J. O., & Hook, F. (2006). Improving the instrumental resolution of sensors based on localized surface plasmon resonance. *Analytical Chemistry*, *78*(13), 4416–4423. https://doi.org/10.1021/ac0601967.

Gaggiotti, S., Hurot, C., Weerakkody, J. S., Mathey, R., Buhot, A., Mascini, M., et al. (2020). Development of an optoelectronic nose based on surface plasmon resonance imaging with peptide and hairpin DNA for sensing volatile organic compounds. *Sensors and Actuators B: Chemical*, *303*, 127188. https://doi.org/10.1016/j.snb.2019.127188.

Hajjar, E., Perahia, D., Debat, H., Nespoulous, C., & Robert, C. H. (2006). Odorant binding and conformational dynamics in the odorant-binding protein. *Journal of Biological Chemistry*, *281*(40), 29929–29937. https://doi.org/10.1074/jbc.M604869200.

Hall, W. P., Modica, J., Anker, J., Lin, Y., Mrksich, M., & Van Duynet, R. P. (2011). A conformation-and ion-sensitive plasmonic biosensor. *Nano Letters*, *11*(3), 1098–1105. https://doi.org/10.1021/nl103994w.

Homola, J. (2008). Surface plasmon resonance sensors for detection of chemical and biological species. *Chemical Reviews*, *108*(2), 462–493. https://doi.org/10.1021/cr068107d.

Hurot, C., Brenet, S., Buhot, A., Barou, E., Belloir, C., Briand, L., et al. (2019). Highly sensitive olfactory biosensors for the detection of volatile organic compounds by surface plasmon resonance imaging. *Biosensors & Bioelectronics*, *123*, 230–236. https://doi.org/10.1016/j.bios.2018.08.072.

Jeanmaire, D. L., & Van Duyne, R. P. (1977). Surface Raman electrochemistry part I. Heterocyclic, aromatic and aliphatic amines adsorbed on the anodized silver electrode. *Journal of Electroanalytical Chemistry*, *84*, 1–20.

Jones, E. M., Balakrishnan, G., Squier, T. C., & Spiro, T. G. (2014). Distinguishing unfolding and functional conformational transitions of calmodulin using ultraviolet resonance Raman spectroscopy. *Protein Science*, *23*(8), 1094–1101. https://doi.org/10.1002/pro.2495.

Jonsson, M. P., Jonsson, P., Dahlin, A. B., & Hook, F. (2007). Supported lipid bilayer formation and lipid-membrane-mediated biorecognition reactions studied with a new nanoplasmonic sensor template. *Nano Letters*, 7(11), 3462–3468. https://doi.org/10.1021/nl072006t.

Jung, J., Chen, L. X., Lee, S., Kim, S., Seong, G. H., Choo, J., et al. (2007). Fast and sensitive DNA analysis using changes in the FRET signals of molecular beacons in a PDMS microfluidic channel. *Analytical and Bioanalytical Chemistry*, *387*(8), 2609–2615. https://doi.org/10.1007/s00216-007-1158-6.

Khan, I., Keshmiri, H., Kolb, F., Dimopoulos, T., & List-Kratochvil, E. (2016). Plasmonic absorber based on multi-diffractive grating. *Advanced Optical Materials*, *4*(3), 435–443.

Langer, J., De Aberasturi, D. J., Aizpurua, J., Alvarez-Puebla, R. A., Auguié, B., Baumberg, J. J., et al. (2019). Present and future of surface-enhanced Raman scattering. *ACS Nano*, *14*(1), 28–117.

Larisika, M., Kotlowski, C., Steininger, C., Mastrogiacomo, R., Pelosi, P., Schutz, S., et al. (2015). Electronic olfactory sensor based on A. mellifera odorant-binding protein 14 on a reduced graphene oxide field-effect transistor. *Angewandte Chemie, International Edition*, *54*(45), 13245–13248. https://doi.org/10.1002/anie.201505712.

Liedberg, B., Nylander, C., & Lundstrom, I. (1983). Surface-plasmon resonance for gas-detection and biosensing. *Sensors and Actuators*, *4*(2), 299–304.

Nespoulous, C., Briand, L., Delage, M. M., Tran, V., & Pernollet, J. C. (2004). Odorant binding and conformational changes of a rat odorant-binding protein. *Chemical Senses*, *29*(3), 189–198. https://doi.org/10.1093/chemse/bjh017.

Neumann, O., Zhang, D. M., Tam, F., Lal, S., Wittung-Stafshede, P., & Halas, N. J. (2009). Direct optical detection of aptamer conformational changes induced by target molecules. *Analytical Chemistry*, *81*(24), 10002–10006. https://doi.org/10.1021/ac901849k.

Pelosi, P., Mastrogiacomo, R., Iovinella, I., Tuccori, E., & Persaud, K. C. (2014). Structure and biotechnological applications of odorant-binding proteins. *Applied Microbiology and Biotechnology*, *98*(1), 61–70. https://doi.org/10.1007/s00253-013-5383-y.

Quilis, N. G., Leveque, M., Khan, I., Knoll, W., Boujday, S., Lamy De La Chapelle, M., et al. (2018). Tunable laser interference lithography preparation of plasmonic nanoparticle arrays tailored for SERS. *Nanscale*, *10*, 10268–10276.

Reiner, A. T., Ferrer, N. G., Venugopalan, P., Lai, R. C., Lim, S. K., & Dostalek, J. (2017). Magnetic nanoparticle-enhanced surface plasmon resonance biosensor for extracellular vesicle analysis. *Analyst*, *142*(20), 3913–3921. https://doi.org/10.1039/c7an00469a.

Sergelen, K., Fossati, S., Turupcu, A., Oostenbrink, C., Liedberg, B., Knoll, W., et al. (2017). Plasmon field-enhanced fluorescence energy transfer for hairpin aptamer assay readout. *ACS Sensors*, *2*(7), 916–923.

Snyder, A. W., & Love, J. (1983). *Optical waveguide theory*. Springer.

Stenberg, E., Persson, B., Roos, H., & Urbaniczky, C. (1991). Quantitative-determination of surface concentration of protein with surface-plasmon resonance using radiolabeled proteins. *Journal of Colloid and Interface Science*, *143*(2), 513–526. https://doi.org/10.1016/0021-9797(91)90284-f.

White, S. A., Briand, L., Scott, D. J., & Borysik, A. J. (2009). Structure of rat odorant-binding protein OBP1 at 1.6 angstrom resolution. *Acta Crystallographica Section D. Structural Biology*, *65*, 403–410. https://doi.org/10.1107/s090744490900420x.

Zhang, D. M., Lu, Y. L., Zhang, Q., Yao, Y., Li, S., Li, H. L., et al. (2015). Nanoplasmonic monitoring of odorants binding to olfactory proteins from honeybee as biosensor for chemical detection. *Sensors and Actuators B: Chemical*, *221*, 341–349. https://doi.org/10.1016/j.snb.2015.06.091.

Zheng, D., Seferos, D. S., Giljohann, D. A., Patel, P. C., & Mirkin, C. A. (2009). Aptamer nano-flares for molecular detection in living cells. *Nano Letters*, *9*(9), 3258–3261. https://doi.org/10.1021/nl901517b.